Monthly Notices of the ROYAL ASTRONOMICAL SOCIETY

MNRAS **500,** 3178–3193 (2021) doi:10.1093/mnras/staa3314
Advance Access publication 2020 October 27

Surface roughness of asteroid (162173) Ryugu and comet 67P/Churyumov–Gerasimenko inferred from *in situ* observations

K. A. Otto [1]★ K.-D. Matz,[1] S. E. Schröder,[1] R. Parekh,[1] K. Krohn,[1] R. Honda, S. Kameda,[2] R. Jaumann,[1,3] N. Schmitz,[1] K. Stephan,[1] S. Sugita,[4,5] E. Tatsumi,[4,6] T.-M. Ho,[7] A. Koncz,[1] F. Trauthan,[1] Y. Cho,[4] M. Hayakawa,[8] C. Honda,[9] T. Kouyama,[10] M. Matsuoka,[8] T. Morota,[4] S. Mottola,[1] K. Ogawa,[8] F. Preusker,[1] N. Sakatani,[2] H. Sawada,[8] F. Scholten,[1] H. Suzuki,[11] M. Yamada,[5] Y. Yokota[7] and K. Yoshioka[12]

[1]*German Aerospace Center, Institute of Planetary Research, Rutherfordstraße 2, D-12489 Berlin, Germany*
[2]*Department of Physics, Rikkyo University, 3-34-1 Nishi-Ikebukuro, Toshima, Tokyo, Japan*
[3]*Institute of Geosciences, Free University of Berlin, Malteserstraße 74-100, D-12249 Berlin, Germany*
[4]*Department of Earth and Planetary Science, University of Tokyo, 7-3-1 Hongo, Bunkyo, Tokyo, Japan*
[5]*Planetary Exploration Research Center, Chiba Institute of Technology, 2-17-1 Tsudanuma, Narashino, Chiba, Japan*
[6]*Instituto de Astrofisica de Canrias, University of La Laguna, Calle Vía Láctea, s/n, E-38205 San Cristóbal de La Laguna, Santa Cruz de Tenerife, Spain*
[7]*German Aerospace Center, Institute of Space Systems, Robert-Hooke-Str 7, D-28359 Bremen, Germany*
[8]*Japan Aerospace Exploration Agency, Institute of Space and Astronautical Science, 3-3-1 Yoshinodai, Chuo, Sagamihara, Kanagawa, Japan*
[9]*Aizu Research Center for Space Informatics, University of Aizu, Aizu-Wakamatsu, 965-8580, Fukushima, Japan*
[10]*National Institute of Advanced Industrial Science and Technology, 2-3-26 Aomi, Koto, Tokyo, Japan*
[11]*Department of Physics, Meiji University, 1-1-1 Higashimita, Tama, Kawasaki, Kanagawa, Japan*
[12]*Department of Complexity Science and Engineering, University of Tokyo, 5-1-5 Kashiwanoha, Kashiwa, Chiba, Japan*

Accepted 2020 October 16. Received 2020 October 6

ABSTRACT

Alteration processes on asteroid and comet surfaces, such as thermal fracturing, (micrometeorite) impacts or volatile outgassing, are complex mechanisms that form diverse surface morphologies and roughness on various scales. These mechanisms and their interaction may differ on the surfaces of different bodies. Asteroid Ryugu and comet 67P/Churyumov–Gerasimenko, both, have been visited by landers that imaged the surfaces in high spatial resolution. We investigate the surface morphology and roughness of Ryugu and 67P/Churyumov–Gerasimenko based on high-resolution *in situ* images of 0.2 and 0.8 mm pixel resolution over an approximately 25 and 80 cm wide scene, respectively. To maintain comparability and reproducibility, we introduce a method to extract surface roughness descriptors (fractal dimension, Hurst exponent, joint roughness coefficient, root-mean-square slope, hemispherical crater density, small-scale roughness parameter, and Hapke mean slope angle) from *in situ* planetary images illuminated by LEDs. We validate our method and choose adequate parameters for an analysis of the roughness of the surfaces. We also derive the roughness descriptors from 3D shape models of Ryugu and orbiter camera images and show that the higher spatially resolved images result in a higher roughness. We find that 67P/Churyumov–Gerasimenko is up to 6 per cent rougher than Ryugu depending on the descriptor used and attribute this difference to the different intrinsic properties of the materials imaged and the erosive processes altering them. On 67P/Churyumov–Gerasimenko sublimation appears to be the main cause for roughness, while on Ryugu micrometeoroid bombardment as well as thermal fatigue and solar weathering may play a significant role in shaping the surface.

Key words: Comets: individual: 67P/Churyumov-Gerasimenko – Minor planets, asteroids: individual: (162173) Ryugu – Planets and satellites: fundamental parameters – Planets and satellites: surfaces – Techniques: image processing..

1 INTRODUCTION

The roughness of airless planetary surfaces is an influential parameter for remote sensing observations of celestial bodies. It has important impact on the photometric behaviour of a surface and therefore influences measurements of reflectance spectroscopy including imagery (Hapke 1984) and thermal emission (Davidsson et al. 2015).

Methods to derive the surface roughness from a planetary body have been developed for various scales. On large scales, roughness is an important parameter for the geologic interpretation of planetary terrains (Helfenstein 1988; Steinbrügge et al. 2020). It also causes effects such as self-heating when light is reflected and radiated to another point on a planetary surface due to the local tilt of the

★ E-mail: katharina.otto@dlr.de

terrain. This can increase local erosion or activity on comets and the Yarkovsky and YORP-effects on asteroids (Keller et al. 2015; Rozitis & Green 2013, 2012). These effects are usually accounted for with a sufficiently high-resolution shape models that have been derived for many planetary missions from image data (Preusker et al. 2019, 2015) or laser altimetry (Barnouin-Jha et al. 2008). The latter allows the derivation of surface roughness from the pulse width of the reflected laser beam (Steinbrügge et al. 2018).

On smaller scales, surface roughness influences the spectral rock signature at wavelengths from the visible to thermal spectrum (Hapke 1981; Davidsson & Rickman 2014). Generally, it is assumed that planetary surfaces are covered with a particulate medium that depending on the particle size and shape influences the reflectance spectra of the observed surface (Hiroi & Peters 1991). However, with increasing spatial resolution of the spectral data the porosity and roughness of the surface material can influence the spectral contrast, spectral shape, and the absolute reflectance/emission due to additional volume scattering and cavity effects (Rost et al. 2018) and should be taken into account in order to avoid a misinterpretation. In addition, the roughness on scales that cause shadowing effects or small-scale self-heating have to be considered when interpreting near-infrared and thermal measurements (Davidsson, Gutiérrez & Rickman 2009). However, only topographic features larger than the thermal skin depth, usually in the centimetre scale, affect these measurements (Davidsson et al. 2015). For example, the thermal skin depth of asteroid Ryugu is approximately 1.5–3 cm (Hamm 2019) and 0.6 cm for comet Churyumov–Gerasimenko (Davidsson et al. 2016).

The Hayabusa2 sample collection procedure revealed that boulders on C-type asteroid Ryugu are covered with a layer of fine-grained particles (<1 mm) that were removed from the boulder surfaces during the collection process (Morota et al. 2020). *In situ* observations of Ryugu as well as comet Churyumov–Gerasimenko reveal that their surfaces are depleted in fine-grained materials and that the majority of surface features are bare rocks or centimetre- to decimetre-sized particle assemblies (Yano et al. 2006; Mottola et al. 2015; Schr"oder et al. 2017a; Jaumann et al. 2019). The rock surface roughness has implications for the shear strength and friction angles of the regolith with higher surface roughness introducing higher friction between the constituents (Reeves 1985; Xu & Sun 2005; Jiang, Li & Tanabashi 2006).

In applied geological sciences, the roughness is often estimated by visually comparing a rock profile with a standard roughness scale (Barton & Choubey 1977). More objective methods involve determining the fractal dimension or the root mean square of the slope distribution (RMS-slope) of rock profiles (Tse & Cruden 1979; Lee, Lee & Park 1997). The RMS-slope is also commonly used as roughness parameter in thermal modelling (Rozitis & Green 2013; Davidsson et al. 2015). Another roughness parameter taking into account more complex surface structures, including overhangs and caves, is the small-scale roughness parameter, which is the geometric measure of the surface area in relation to its flat projected area (Lagerros 1997; Davidsson & Rickman 2014)

In this work, we will extract roughness parameters from the only two surfaces of small bodies imaged *in situ*: asteroid Ryugu and comet Churyumov–Gerasimenko. This allows us to derive the millimetre scale roughness measured over a horizontal scale of a few tens of centimetres of the two volatile-rich bodies, compare them quantitatively and discuss the different alteration processes' influence on the surface structure. To gain insight of the dependence of roughness on the spatial scale, we also apply our method to two global images from Ryugu and Churyumov–Gerasimenko. By doing so, we avoid any influence that the method of derivation may have on the result.

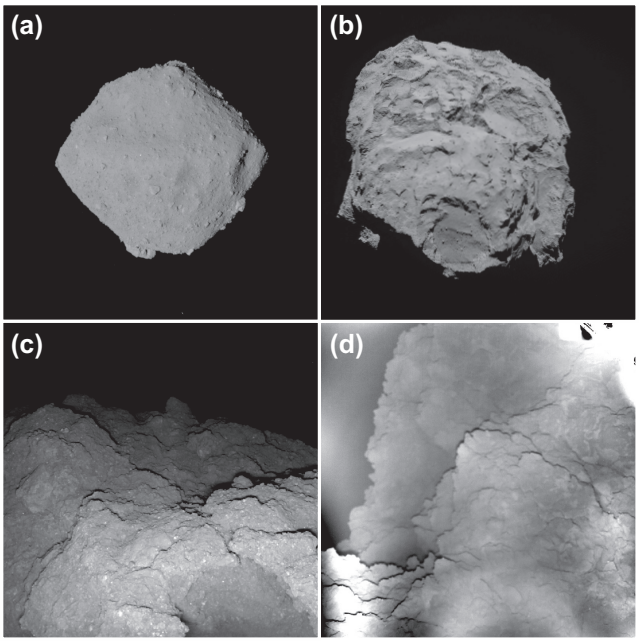

Figure 1. Asteroid Ryugu and comet 67P/Churyumov–Gerasimenko imaged from orbit (upper row) and *in situ* (lower row). (a) Ryugu is approximately 900 m in diameter. (b) Churyumov–Gerasimenko from a frontal view with the small lobe in front of the big lobe (∼2.5 km across). (c) *In situ* image of Ryugu illuminated with MasCam's red LED. The scene is approximately 25 cm across. The darker appearing area in the lower right corner is a cave (∼7 cm wide). (d) *In situ* image at Philae's second landing site on Churyumov–Gerasimenko illuminated with ROLIS' red LED. The scene is approximately 80 cm across. Stray light is clearly visible as alternating light and dark circular areas originating from the lower edge of the image. The overexposed feature in the top right is caused by Philae's leg.

In the following sections, we first summarize the space mission operation at Ryugu and 67P and their main observations (Section 2), followed by a detailed description of the data used in this work (Section 3). In Section 4, we introduce the roughness parameters and methods developed to extract them. Section 5 includes an analysis of the model parameters and summarizes the roughness parameters of Ryugu and 67P. Section 6 discusses the influence of the model parameters and possible formation mechanisms of surface roughness. Finally, a discussion of the wider context of the results and its conclusion is given in Sections 7 and 8, respectively.

2 *IN SITU* OBSERVATIONS

Before deriving roughness parameters for Ryugu and Churyumov–Gerasimenko, we first introduce the general scene of the landing sites.

2.1 Scene of the MASCOT landing site

In 2018 June, JAXA's Hayabusa2 mission rendezvoused with Cb-type near-Earth asteroid Ryugu (Watanabe et al. 2017, 2019). Ryugu is a top-shaped asteroid of approximately 950 m diameter (Fig. 1a). Its relatively low density of 1.19 g cm^{-3} suggests a high bulk porosity (>50 per cent) and rubble pile structure (Watanabe et al. 2019). Ryugu is relatively dark with a geometric albedo of 4.0 per cent at 0.55 μm (Sugita et al. 2019; Tatsumi et al. 2020) and has been

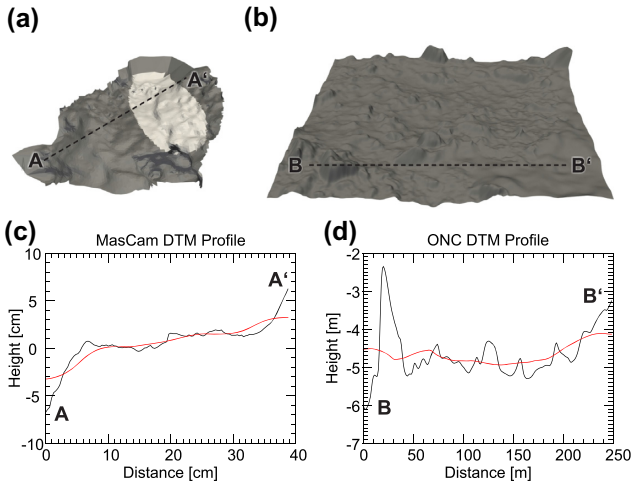

Figure 2. The 3D shape models used in this work and representative profiles. (a) The MasCam shape model from the *in situ* observation of Ryugu. The scene is approximately 25 cm across and a facet is about 3 mm wide. The light-shaded area is the MARA footprint. (b) ONC DTM of the area around Mascot's landing site (50 m × 50 m at 20 cm spatial resolution). (c and d) Profiles through MasCam and ONC DTM (the black lines) as indicated in (a) and (b), respectively. The red line is the reference surface.

linked to CI or CM meteorites (Jaumann et al. 2019; Kitazato et al. 2019; Sugita et al. 2019). The surface and regolith appear rough, covered with rocks and boulders of various sizes and shapes (Sugita et al. 2019), while smaller particles in the sub-centimetre size range and dust are missing (Jaumann et al. 2019). Four morphologic types of boulders have been identified (Sugita et al. 2019): the unique bluish boulder Otohime Saxum near the south pole, bright and mottled, bright and smooth, and dark and rugged boulders. The last two types have also been observed by the Mobile Asteroid Surface Scout (MASCOT) during its descent and the rugged boulder type has additionally been observed *in situ* in high image resolution on Ryugu's surface (Fig. 1c).

MASCOT was detached from the Hayabusa2 spacecraft on 2018 October 3 and after the initial descent phase and relocation on the surface, MASCOT landed near a crumbly and rough boulder that it observed *in situ* with four on-board instruments [Jaumann et al. 2019; camera, radiometer, magnetometer, and spectrometer (unable to return expected data; Ho et al. 2017)] including a high-resolution camera (MasCam; Jaumann et al. 2017). Due to a slight tilt towards the surface (22° with respect to the surface plane), a field of view of 55° and the Scheimpflug optics of MasCam, resolutions down to 0.15 mm could be achieved in the lower part of the images while at the same time maintaining image sharpness for larger distances. Additionally, MasCam was equipped with an LED array composed of four individual colours (blue, green, red, NIR) for illumination during night time. A mini-move by MASCOT allowed observing of the scene from two different directions, which was used to derive a 3D shape model of the observed rough boulder on a spatial scale down to ∼3 mm (Fig. 2a; Scholten et al. 2019).

MasCam showed a scene, approximately 25 cm across, highlighting a bare boulder with bright inclusions in the millimetre scale, but visible absence of sand and pebble-sized particles (Jaumann et al. 2019). This in combination with the radiometric measurements led to the conclusion that the boulder is highly porous (28–55 per cent) and that the tensile strength is relative low (200–280 kPa; Grott et al. 2019). In fact, small pores larger than 1 mm could not be observed while smaller pores may be present but not resolvable within the MasCam image (Grott et al. 2019). The 3D scene shows a prominent hollow in the foreground with a size of approximately 7 cm with multiple smaller indentations (∼2 cm) and a roughly 2 cm extended overhang at the right-hand corner of the scene (Fig. 1c). The hollow and indentations have a convex shape. Cauliflower-like undulations on the scale of ∼1 cm form the surface texture of the boulder. They are covered with further, smaller undulations of approximately 2–3 mm, which suggest a fractal nature of the surface. Although there are exceptions, the feature size of 1 cm and 2–3 mm appears to be a characteristic for this scene.

The images of MasCam show a cauliflower-like rock surface texture, which can also be observed for cohesive fine-grained materials. This is particularly evident in the images acquired during night when the LEDs were used to illuminate the surface. This structural appearance resembles pristine cometary material observed *in situ* by the Philae lander comet Churyumov–Gerasimenko (Bibring et al. 2015; Schr"oder et al. 2017a) and is also similar to fracture surfaces of aqueously altered carbonaceous chondrites (Fuchs, Olsen & Jensen 1973; Gounelle & Zolensky 2014). We will discuss the similarities and differences between Ryugu's and Churyumov–Gerasimenko's surface texture in more detail in this work.

2.2 Scene of the ROLIS landing site

On November 12, the Philae lander on board the Rosetta mission was detached and landed on comet Churyumov–Gerasimenko (Ulamec et al. 2016). After the initial touchdown and bounce, Philae got to rest at the Abydos site, a relatively rough terrain on the comet. Churyumov–Gerasimenko is a bi-lobate Jupiter family comet with dimensions 4.3 km × 2.6 km × 2.1 km (Jorda et al. 2016). With an estimated bulk porosity of 70–75 per cent (Jorda et al. 2016), Churyumov–Gerasimenko is more porous than asteroid Ryugu. Churyumov–Gerasimenko is relatively dark with a geometric albedo of 6.2 per cent at 0.55 μm (Ciarniello et al. 2016). Geomorphologically, Churyumov–Gerasimenko possesses a north–south dichotomy exhibiting a rough consolidated terrain in the south and a smooth airfall-covered terrain in the north. This is probably caused by the increased erosion of the Southern hemisphere during the perihelion passage (Keller et al. 2015). The rough terrain of the Southern hemisphere, where Philae came to its final rest, is composed of consolidated material of 10–50 cm thickness (Knapmeyer et al. 2018). This layer probably formed by sintering and cementing of volatiles and dust in the near surface layers (Spohn et al. 2015). Two camera systems on-board Philae, CIVA, and ROLIS, showed this consolidated rough terrain in detail (Poulet et al. 2016; Schr"oder et al. 2017a). Similar to MasCam on Ryugu (Jaumann et al. 2019), CIVA reports on two types of textures within the field of view – a smooth fine-grained and a rough granular texture (Poulet et al. 2016). ROLIS describes a consolidated jagged surface with cracked plates. Schr"oder et al. (2017a) also note the fractal nature of Churyumov–Gerasimenko's surface by describing similar surface morphologies on various scales.

The ROLIS camera on-board Philae operated in a similar manner to MasCam on Ryugu. Both cameras possess a 1024 m × 1024 sensor and a four colour LED array [465–812 nm (MasCam), 470–870 nm (ROLIS)] for illuminating the near surface (Mottola et al. 2007; Jaumann et al. 2017). ROLIS was mounted underneath the Philae lander and was focusing on a surface 30 cm away from the lens. At this distance, the field of view of 58° has a pixel resolution of 0.33 mm (Mottola et al. 2007). However, as Philae landed on its side and thus ROLIS partly pointed to the horizon ROLIS' infinity lens, aimed to be employed for long distances during descent, yielded

the best image of the scene on Churyumov–Gerasimenko (Schr"oder et al. 2017a).

ROLIS showed an approximately 80 cm × 80 cm scene at Philae's second landing site on comet Churyumov–Gerasimenko (Fig. 1d). Similar to Ryugu, no individual grains or pebbles were detected on the surface, but some ejected particles were visible moving along the horizon (Schr"oder et al. 2017a). A bimodal brightness distribution with dark smooth patches and bright areas running along rough edges are visible. The albedo variation has been suggested to be the result of different degrees of consolidation of the same material with the light areas being less consolidated compared to the dark areas. The surface also appears to have no visible inclusions or pores above ∼1 mm in size (Schr"oder et al. 2017a). The surface morphology of Churyumov–Gerasimenko appears similar to Ryugu with cauliflower-like patterns and undulations, but of slightly larger extent of ∼5 cm. The cometary structure seems somewhat more ragged, illustrated by small ∼1 cm slots and pointy ridges.

3 DATA

3.1 MASCOT on Ryugu

We used *in situ* images acquired by MasCam at the second landing site at 22°S and 317°E (Jaumann et al. 2019). At this location, the main science cycle was conducted and day and night time images were taken. For the evaluation of roughness, we chose the image acquired during night time illuminated with the red LED (image tag: F1087378791_701_29464_r2, exposure time: 3 ms, image depth: 14 bit) as the stray light in this image appears the least prominent (Schr"oder et al. 2020) and the contrast highest compared to the other illumination colours (Fig. 1c). This image is 1024 × 1024 pixels large and has a pixel resolution of approximately 0.2 mm across the foreground of the image which is the focus of our analysis. A geometric correction of the image was not applied as the effects are negligible.

A shape model of the scene observed by MASCOT and a 50 m × 50 m large shape model with a spatial resolution of 20 cm and 124000 facets derived from Hayabusa2's optical navigation cameras (ONC) images of MASCOT's landing site (Preusker et al. 2019; Scholten et al. 2019) were used to independently derive the RMS-slope and small scale roughness parameter for comparison with our method (Fig. 2).

3.2 Philae on 67P/Churyumov–Gerasimenko

We analyse the roughness of a cometary rock using images taken on Churyumov–Gerasimenko by the ROLIS camera on-board the Philae lander on Rosetta (Mottola et al. 2007). However, the ROLIS images are highly affected by stray light introduced by the lens system and an overexposed part of the lander foot in one corner of the image. Thus, we used the enhanced and processed red image published by Schr"oder et al. (2017a) for our analysis (Fig. 1d). The image is slightly out of focus, however, as we will see below (Section 4.2) this will not affect our conclusions. The pixel resolution of this image is approximately 0.8 mm in the foreground with a total of 1024 × 1024 pixels.

3.3 Global analysis

Finally, we used two global images acquired with the red filters of the orbiter cameras on-board Hayabusa2 (ONC-T; Kameda et al. 2017) and Rosetta (OSIRIS; Keller et al. 2007) to extract large-scale roughness values with our method (Fig. 1a and b). The image of Ryugu (image tag: hyb2_onc_20180925_091520_twf_l2d) has an image depth of 10 bit and a size of 1024 × 1024 pixels. For validating the quality of our method, we also used the blue version of this image that was taken a minute after the red image and is visually almost identical to the red image (image tag: hyb2_onc_20180925_091624_tbf_l2d). The image of Churyumov–Gerasimenko (image tag: NAC_2014-08-06T01.20.01.282Z_ID30_1397549600_F28) has an image depth of 14 bit and is with 2028 × 2048 pixels twice as large as the other images used in this work. Both images have a spatial resolution of approximately 2 m. Here, we chose an image showing a frontal view of Churyumov–Gerasimenko to avoid the bi-lobate shape of the comet to influence our results. Both global images are geometrically corrected to minimize large-scale distortion effects on the analysis.

4 METHOD

In this work, we report on the topographic surface roughness on asteroid Ryugu and comet Churyumov–Gerasimenko from space mission images. We introduce a new objective and reproducible method to extract eight commonly used roughness parameters including the RMS-slope, hemispherical crater density, fractal dimension, Hurst exponent, JRC, small-scale roughness parameter, and Hapke mean slope angle from such images. Before describing the method (Sections 4.2 and 4.3), we first introduce the roughness parameters in detail (Section 4.1).

4.1 Description of roughness parameters

4.1.1 RMS-slope

The RMS-slope distribution of a planetary surface can be derived when the topography of a body is known. Given a local or global shape model composed of N connected facets, the RMS-slope s is defined as the root of the square of each facet's slope θ_i weighted by the projection of the facet area a_i on to the local reference plane (Spencer 1990; Rozitis & Green 2011; Davidsson et al. 2015):

$$s = \sqrt{\frac{\sum_{i=1}^{N} {\theta_i}^2 a_i \cos\theta_i}{\sum_{i=1}^{N} a_i \cos\theta_i}}. \quad (1)$$

In order to assess spatially unresolved roughness of remote sensing data from space missions, specifically those of thermal infrared emission observations, various roughness models have been established (Davidsson et al. 2015). A commonly used model assumes that the unresolved roughness can be represented by a flat surface speckled with spherical-section craters (Buhl, Welch & Rea 1968; Spencer 1990). The parameters defining the roughness are the crater density f and the ratio between crater depth and crater curvature diameter $\delta = \frac{1}{2}(1 - \cos\gamma)$, where γ is the largest slope angle of the crater. The RMS-slope is then defined as (Lagerros 1996; Davidsson et al. 2015):

$$s = \sqrt{\frac{f}{2}\left(\gamma^2 - \frac{(\gamma\cos\gamma - \sin\gamma)^2}{\sin\gamma^2}\right)}. \quad (2)$$

The RMS-slope in this model depends on two parameters f and γ, however, in many cases of modelling roughness on airless bodies, hemispherical craters are assumed ($\gamma = 90°$, $\delta = 0.5$) so that the

RMS-slope simplifies:

$$s_{\delta=0.5} = \sqrt{\frac{f}{2}\left(\frac{\pi}{4} - 1\right)}. \tag{3}$$

A saturation of hemispherical craters results in an RMS-slope of 49°. This model has also been applied by Grott et al. (2019) when calculating the thermal conductivity of the boulder observed on Ryugu from thermal infrared measurements. A hemispherical crater density of $f = 0.34$ represents a good agreement with their measurement. On Churyumov–Gerasimenko, the hemispherical crater density is highly dependent on the geologic setting and varies between 0.1 and 0.8 (Marshall et al. 2018). For comparability, we will also use the hemispherical crater density in this work.

4.1.2 *Small-scale roughness parameter*

The small-scale roughness parameter ξ describes the ratio between the area of a rough surface a_r and its projection on to a reference surface a_p (Davidsson et al. 2009; Davidsson & Rickman 2014):

$$\xi = 1 - \frac{a_p}{a_r}. \tag{4}$$

The advantage of this parameter is that it considers the contribution of cavities and overhangs of a rough surface that cannot be represented by the RMS-slope. It approaches 1 for very rough surfaces. For some thermal roughness models, including the crater roughness model described above, the small-scale roughness parameter is identical to the small-scale self-heating parameter when scattering is neglected (Davidsson & Rickman 2014; Lagerros 1998, 1997). Using a thermophysical model reproducing temperatures extracted from the near-infrared spectrum of comet 9P/Tempel 1, Davidsson et al. (2009) found that small-scale self-heating parameter values between 0.6 and 0.75 are common for the comet and values as low as 0.2 were also found in smoother areas.

4.1.3 *Hapke mean slope angle*

Another popular roughness parameter, commonly used in spectral investigations of remote sensing data, is the Hapke mean slope angle $\bar{\theta}$ of a rough surface. Hapke (1984) assumes that the roughness is introduced by flat facets with normally distributed orientations and defines the Hapke mean slope angle of these facets as

$$\tan\bar{\theta} = \frac{2}{\pi}\int_0^{\pi/2} \tan\theta a(\theta)\mathrm{d}\theta, \tag{5}$$

where a is a normalized Gaussian distribution of not too large slope angles θ. Following Lagerros (1997), the relationship between Hapke's mean slope angle and the small-scale roughness parameter ξ (equation 4) can be expressed as

$$\xi = 1 - \frac{E_1(\cot^2\bar{\theta}/\pi)}{\pi\tan\bar{\theta}\,\mathrm{erfc}(\cot\bar{\theta}/\sqrt{\pi})}, \tag{6}$$

if the slopes follow a Gaussian distribution. Here, $E_1(x) = \int_1^\infty \exp(-xt)/t\ \mathrm{d}t$. In the roughness regime of most planetary surfaces ($\bar{\theta} \approx 20°$–$40°$), the relationship between ξ and $\bar{\theta}$ is nearly linear with a slope of 0.009 [1/°] (Fig. 3).

As we will see later, the criterion that the slope distribution is normally distributed is a consequence of the method we will apply and this assumption is therefore valid. However, the constraint to small angles will pose some difficulties as we will discuss in Section 7.

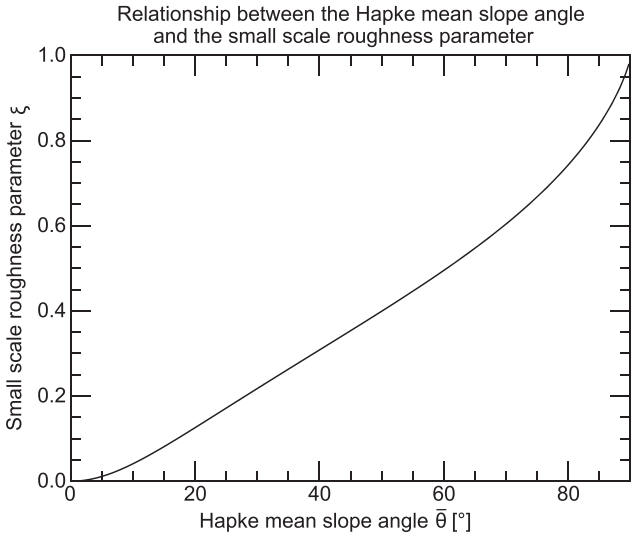

Figure 3. Relationship between the Hapke mean slope angle and small scale roughness parameter (equation 6). The relationship is approximately linear in the regime of most planetary surfaces with $\xi \approx 0.009[1/°] \cdot \bar{\theta}$.

4.1.4 *Fractal dimension, Hurst exponent, and joint roughness coefficient*

The fractal dimension is a measure of the surface roughness of self-affine structures (Zahouani, Vargiolu & Loubet 1998). Fractal surfaces possess the characteristic that with decreasing measuring unit r the total length of the measured surface L increases monotonically (Mandelbrot 1967; Huang, Oelfke & Speck 1992):

$$L(r) = r^{D-1}, \tag{7}$$

where D is the fractal dimension, which varies between 1 for smooth and 2 for rough 2D surfaces. Fractal descriptions have been found to be useful in various geologic applications including the description of coastlines and the joint surfaces of rocks (Mandelbrot 1967; Odling 1994).

The fractal dimension is dependent on the dimension of the space, e.g. 2D or 3D, it has been determined for. The Hurst exponent H is linearly related to the fractal dimension, independent of the dimension of space and varies between 0 and 1 for smooth and rough contours/surfaces, respectively (Shepard & Campbell 1998):

$$H = 2 - D \qquad \text{(for 2D profiles)}, \tag{8a}$$

$$H = 3 - D \qquad \text{(for 3D surfaces)}. \tag{8b}$$

A way to construct such a fractal surface is the Koch curve. Starting with a straight line segment, a triangle with base length l and height h is placed in the centre of the line forming the first-order Koch curve. The repetition of this procedure on each of the first-order line segments generates the second order and so on, creating a fractal structure. In geoscientific applications, natural rock joints are often assumed to follow a construction similar to the Koch curve (Xie & Pariseau 1994). The advantage is that the fractal dimension can be estimated from a single length-scale of a 2D contour using the equation

$$D = \frac{\log 4}{\log\left(2\left(1 + \cos\left(\tan^{-1}\left(2h/l\right)\right)\right)\right)}, \tag{9}$$

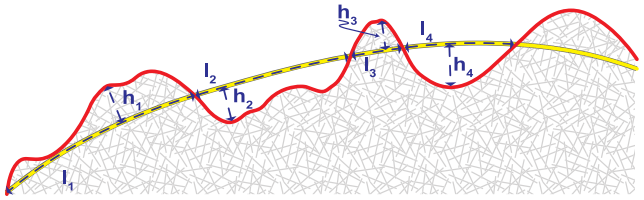

Figure 4. Illustration of the derivation of the fractal dimension of a 2D profile. Shown is the measurement (the blue-dashed lines) of base length and asperity height of a natural contour (the red line). The reference contour is sketched as the yellow line.

where h and l are the average height and the base length of high-order asperities of a rock joint (Xie & Pariseau 1994; Li & Huang 2015; Fig. 4). The fractal dimension of the equilateral Koch curve with $h = \sqrt{3/2}l$ yields $D = \log 4/\log 3 = 1.26$.

The fractal dimension can be correlated to the joint roughness coefficient (JRC), a measure of the roughness of rock joints used to estimate the peak shear strength of a material. The JRC has been empirically related to the fractal dimension by the formula (Li & Huang 2015)

$$\mathrm{JRC} = 118.89(D-1)^{0.4343}. \tag{10}$$

The peak shear strength τ of a joint rock surface is given by

$$\tau = \sigma_\mathrm{n} \tan\left(\mathrm{JRC}\log\left(\frac{\mathrm{JCS}}{\sigma_\mathrm{n}}\right) + \Phi_\mathrm{b}\right), \tag{11}$$

where σ_n is the effective normal stress, JCS is the joint wall compressive strength, and Φ_b is the basic friction angle (Barton 1976). Note that both, τ and σ_n, have the unit of a pressure.

4.2 Roughness from 2D images

To extract the surface roughness from images acquired *in situ* on asteroid Ryugu and comet Churyumov–Gerasimenko with the highest available spatial resolution, we derive the RMS-slope, hemispherical crater density, small-scale roughness parameter, Hapke mean slope angle, fractal dimension, Hurst exponent, and JRC from the outline of imaged rocks applying an objective and reproducible method suitable for images acquired with LED illumination. Due to its high quality and resolution, we tested our method and its dependence on the input parameters using the MasCam image (Section 5.1).

Our method is based on the observation that the texture and material imaged is relatively homogeneous over an area smaller than the rock but large enough to be statistically relevant (>1000 pixels). Within the illuminated images, it can be assumed that parts of the rock with the same distance to the LED have a similar radiance and that with increasing distance the radiance decreases ($\propto r^2$). This makes areas with the same distance from the camera similarly bright in the image. Thus, we aim at determining the 2D surface at a specific distance, represented by pixels of similar radiance. It can be imagined as a cut through the rock perpendicular to the camera at a specific distance. The texture caused by bright or dark inclusions and varying surface tilts at this specific distance is considered by computing the histogram of pixel brightness values at the given distance and by assuming a Gaussian distribution of these pixel values. The mean and variance of this distribution allow constraining pixels belonging to a specific distance by their brightness values.

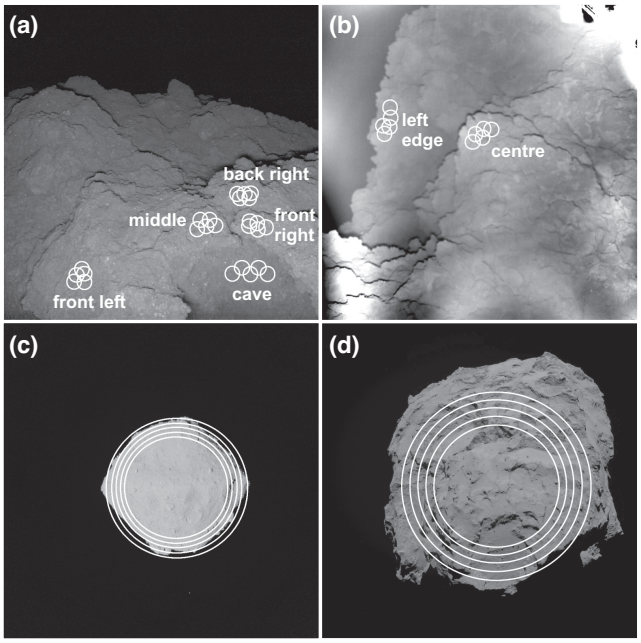

Figure 5. The four images used in this work. Each region to be analysed (labelled in upper row) was investigated using five slightly varying starting regions (the white circles). Note that the number of regions investigated in each image varies and that a different starting region selection procedure was applied for the global images. Here, the size of the starting regions varies with the smaller starting regions being a subset of the larger ones, whereas the *in situ* images have overlapping staring regions of the same size. (a) The red MasCam image of Ryugu (∼0.2 mm spatial resolution). (b) The red ROLIS image of Churyumov–Gerasimenko (∼0.8 mm spatial resolution). Note the stray light emerging from the lower image boundary as quasi-circular alternating light and dark regions. The starting regions were chosen in areas that are less dominated by stray light. (c) ONC image of Ryugu at ∼2 m spatial resolution. (d) OSIRIS image of Churyumov–Gerasimenko at ∼2 m spatial resolution.

More precisely, looking at the *in situ* images (Fig. 5a and b), for each image investigated we identified structures [labelled front left, middle, cave, front right, and back right on Ryugu and left edge and centre on Churyumov–Gerasimenko (Fig. 5a and b)] of which to measure the surface roughness. Where available, we also used a shape model to make sure that the structures had a more or less constant distance to the camera. Within these structures, we defined five circular starting regions that covered a representative texture and colour of the structure to investigate (Fig. 5). The regions comprised ∼1835 pixels within the *in situ* images. Within the MasCam image this corresponds to a roughly 1 cm in diameter circle on the rock surface. For each structure, we derived the roughness parameters by growing all of the five circular starting regions using a standard growing algorithm (see below for details) and averaged the results to generate a representative value.

We also used two global images of Ryugu and Churyumov–Gerasimenko to derive the roughness parameters on a larger scale. For these, we used a slightly different approach taking advantage of the fact that the background of the images is black space and therefore easily distinguishable. The five circular starting regions covered the majority of the imaged object (Fig. 5c and d). Comprising dark pixels showing space in the circular starting regions, results in a pixel value histogram with two peaks, one at the average asteroid/comet pixel value and one at the average space pixel value, which would allow a precise determination of the object's limb. However, we used circular

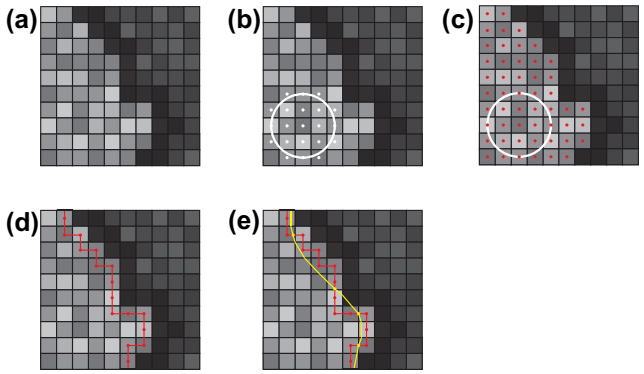

Figure 6. Sketch illustrating the method used in this work. (a) Image composed of pixels with lighter area to the left separated from a darker area to the right by a dark shadow. (b) Starting region in the light area. The large white circle illustrates the starting region. Pixels with the white dots belong to the starting region. (c) The grown region marked by the red dots. (d) Boundary pixels (the red dots) and their connection (the red lines). (e) Boundary contour (red) and reference contour (yellow). The yellow dots illustrate the boundary between adjacent sections as needed for deriving the fractal dimension (compare with Fig. 4b).

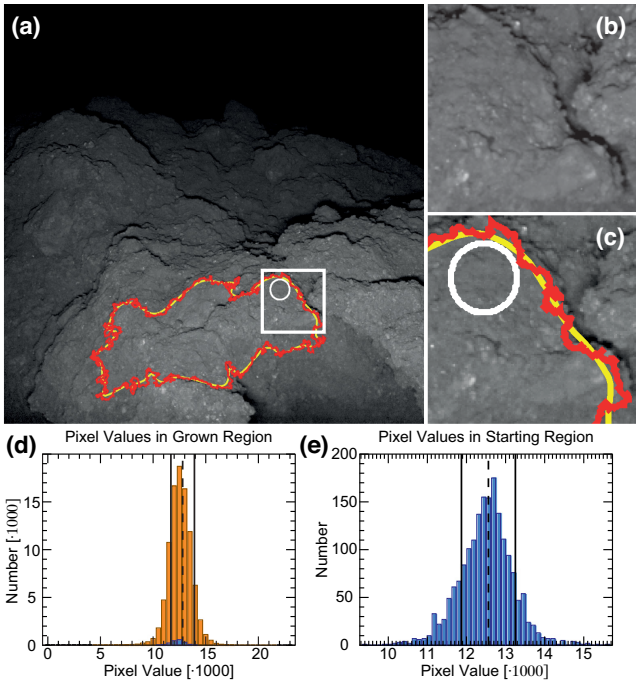

Figure 7. Illustration of the growing region algorithm in the middle of the MasCam image. (a–c) The MasCam image with circular starting region (white), rough detected outline (red), and smoothed reference contour (yellow). (b) and (c) are subsets of (a) as indicated by the white box. Note that the rough outline follows the shadow detected closest to the starting region rather than the most prominent one. (d) Histogram of all pixel values within the grown region. The blue histogram represents the histogram of the starting region as shown in (e). The dashed and dash–dotted lines indicate the mean and the 1standard deviation, respectively.

starting regions that predominantly cover the object to be consistent with the approach used for structures in the *in situ* images. The five circular starting regions had varying sizes ranging from 0.5–1.2 $\times$ 10^6 pixels for Churyumov–Gerasimenko and 0.8–1.4 $\times$ 10^5 for Ryugu. Each smaller circular staring region was a subset of the larger ones.

We then grew each of these regions using a region growing algorithm. Figs 6 and 7 illustrate our method. We determined the mean and standard deviation of the pixels' values within each circular starting region (7e) and added all connected neighbouring pixels (each pixel has eight neighbours) that had radiance values falling within the mean plus/minus a multiple of the standard deviation to the region (Figs 6c and 7e). Pixels not fulfilling this criteria but being surrounded by pixels fulfilling it were also considered part of the grown region. In general, we constrained the values using one standard deviation around the mean, but also investigated the effect when changing this range (Section 5.1). The boundary of this grown region was then used as the structure's boundary profile. The boundary pixels are connected in a closed loop (the red line in 7a) with each boundary pixel having exactly one preceding and one following neighbour within the eight surrounding pixels (6d).

Although in some cases, specifically the MasCam observations, the image quality appears relatively good the roughness on the pixel scale is not solely introduced by the topography of the rock surface. Instead effects such as image noise, point spreading of particularly bright features, and rock texture introduce a roughness to the rock surface that needs to be neglected when deriving the topographic roughness. In order to remove such factors, we applied a morphologic operator to the grown region. By mathematically closing the grown region with a circular structural element (dilation followed by erosion), we filled indentations of the size of the structural element along the contour boundary (e.g. Gonzalez & Woods 2018). This process also counteracts any biases arising from blurry image boundaries.

Inclusions are the most prominent disturbance along the boundary within the rocks on Ryugu. Their size ranges from 0.1 to 2 mm with a characteristic size of 3 pixels in the area investigated. We therefore chose the size of the structural element for the closing operation to be 3 pixels across, but also investigated the influence of different sizes of the structural element.

To derive the above described roughness parameters from the boundary, a reference contour is needed. This reference contour represents the assumed local rock topography without any roughness. Although all roughness parameters depend on this reference contour, it is often chosen arbitrarily in the literature. Here, we derived the reference contour by applying a running mean along the rough boundary contour. For each point along the boundary, we derived the mean x–y position including the preceding 50 and following 50 pixels along the boundary. Within the MasCam images, 100 pixels correspond to roughly 2 cm length, which is an appropriate length-scale given the size of indentations and overhangs described in Section 2.1. This smoothened boundary was used as the reference contour (Figs 6e, and 7a and c). We also experimented with changing the length of the running mean. Note that the constraint formulated by Hapke (1984), that the slope angles follow a Gaussian distribution (Section 4.1.3), is automatically fulfilled when applying a running mean to define the reference contour.

Given the reference contour and the rough boundary contour of a specific structure identified in the high-resolution images, we derived the RMS-slope of the rough contour by determining the angle between the line connecting two adjacent pixels along the rough boundary contour and the line connecting the corresponding pixels on the reference contour. Following equation (1), we derived the RMS-slope from this angle and the length of the section between the two adjacent pixels on the rough contour. Because the derivation of the RMS-slope requires a 3D surface boundary rather than a 2D surface

contour, we assumed that the depth of the pixel along the direction of the boresight vector is the same as the pixel dimension in the image, e.g. 1. This allowed us to simply use the distance between two pixels as the facet area required in equation (1). Using the angle between the reference and rough boundary contour as described above and again assuming that the extent of the pixels along the boresight vector is 1, we derived the small-scale roughness parameter by projecting the rough boundary segment on to the reference contour and applying equation (4).

Finally, we derived the fractal dimension of the rough boundary contour with respect to the reference contour by finding the intersections of the rough boundary contour and the reference contour. For each section bounded by two adjacent intersections (Fig. 6e) we derived the base length by calculating the distance between the two adjacent intersections along the reference contour and the local height by calculating the maximum distance of any rough boundary pixel located in this section to the reference contour (Fig. 4b). We then derived the fractal dimension applying equation (9) by repeating these calculations for each section bounded by two adjacent intersections and determining the average base length and height from all sections. We then applied equation (10) to estimate the JRC.

4.3 Roughness from 3D shape models

Additionally, we derived the roughness parameters from two local shape models. For a comparison with the roughness estimated by fitting thermal measurements (Grott et al. 2019), we considered the roughness of the MARA footprint in the MasCam DTM separately. As reference surface we used an arbitrary sphere. Note that the radius of this sphere is not necessary to determine because the angle between a facet's and the sphere's local normal vectors is independent of the radius of the sphere.

Furthermore, we determined the fractal dimension and corresponding Hurst exponent and JRC for these differently resolved shape models near the MASCOT landing site. These parameters are derived from 2D contours. Thus, we extracted 10 arbitrary profiles each and calculated the reference contour for the 20 cm resolution ONC DTM by smoothing the profiles consisting of 250 data points (50 m) with a running mean of 100, which corresponds to approximately 20 m, maintaining the same ratio between the DTM spatial resolution and smoothing resolution (0.01) as applied in the image-based method described above. Due to the small length of the profiles of the 3 mm resolution MasCam DTM (53–121 data points, 16–39 cm), the smoothing factor was chosen to be 34 (10 cm), which is on average the same ratio between profile length and smoothing factor as chosen for the ONC DTM, and thus maintains comparability. Profiles crossing through the cave in the front of the MasCam DTM were not considered due to restrictions of our 2.5D profile extraction tool. To derive a representative fractal dimension, Hurst exponent and JRC we averaged the results from the individual profiles. The so-derived 2D fractal dimension is comparable to the 3D value (Tatone & Grasselli 2009; Cai et al. 2018)

5 APPLICATION AND RESULTS

5.1 Effect of input parameters on roughness

In order to access the reliability of our results and its sensitivity to the chosen parameters, we used the basic parameter set as described in Section 4.2 for the middle region in the MasCam image (smoothing factor of reference contour = 100, standard deviation multiplier = 1, size of structural element = 3, image pixel resolution = 1) and varied one parameter at a time. The result is summarized in Table 1.

To explore the robustness of our method against image noise, we added a Gaussian random noise to the MasCam image with a scale factor of 10 per cent and 50 per cent of the mean pixel value of the image. As shown in Fig. 8, the area detected by the grow region algorithm varies slightly in the 10 per cent noise image (Fig. 8b) and expands to the right-hand side in the 50 per cent noise image (Fig. 8c) compared to the original image (Fig. 8a). This can be explained by noisy pixels bridging shadows and allowing the algorithm to grow into areas that are separated by a shadow in the image without or little noise. We then extracted the roughness values and found that the RMS-slope and corresponding hemispherical crater density slightly decrease (for 10 per cent noise level) and increase (for 50 per cent noise level) when introducing noise, but they agree within their errors. The fractal dimension and derived values (Hurst exponent and JRC) show the opposite effect of a very small increase in roughness for a 10 per cent noise level and a decrease for 50 per cent noise level. This decrease can be explained by the growing region reaching the image border to the right and therefore artificially detecting a flat boundary. The small-scale roughness parameters and Hapke mean slope angles are constant within their errors. This inconsistency in roughness variation and the low variation within the derived roughness values with additive noise shows that the image noise does not have a systematic effect on the roughness derived. This is achieved by the mathematical closing of the detected boundary, which effectively erases any noise along the boundary on the scale of the structural element.

The filters and camera settings also have an effect on the point spread function on the detector and therefore on the quality of an image. The point spread function is dependent on the incident angle, camera temperature, and wavelength. We investigated whether the wavelength influences the result of our method by repeating the global analysis of Ryugu with a blue Ryugu image taken a minute after the red image shown in Fig. 5(c). Both, the red and blue image, are visually nearly identical and so we used the exact same starting region locations. The roughness derived from the blue and red images are either identical or agree within 1σ standard deviation. We thus conclude that the wavelength the image was taken at and the according point spread function does not have a significant effect on the roughness derived from an image.

The smoothing factor to generate a reference contour was chosen to be 100, e.g. a running mean of 100 points was applied to the boundary surface. Increasing this number results in a smoother and decreasing in a rougher, more similar to the boundary surface, reference contour. The RMS-slope and corresponding hemispherical crater density increase steadily with increasing smoothing factor. This behaviour is expected because the reference contour's similarity to the boundary contour decreases with increasing smoothing factor and therefore results in a higher roughness. A similar trend is observed for the small-scale roughness parameter and Hapke mean slope angle with an exception for the highest smoothing factor of 300, which is the lowest value. However, the error on this value is comparatively large and points at an outlier within the individual starting regions' results. The fractal dimension and derived parameters (Hurst exponent and JRC) show no obvious trend with increasing smoothing factor. The more similar the reference contour is to the boundary contour (e.g. the smaller the smoothing factor), the more intersections of the reference and boundary contour exist and the more values for the average section length and height can be taken into consideration generating a larger statistic, but not necessarily different values. Thus, a smoothing factor of 100 is reasonable for the scene observed.

Table 1. Parameters describing the roughness of the rock on Ryugu derived directly from the *in situ* image for the representative region in the middle of the image. The effect of different input parameters on the derived roughness parameters is shown. The errors are the 1σ standard deviation derived from five locally varying starting regions and, where deduced from other values, derived via standard error propagation.

Input				Result						
Standard deviation multiplier	Size of structural element	Image resolution	Smoothing factor reference contour	RMS slope (°)	Hemispherical crater density	Fractal dimension	Hurst exponent	JRC	Small scale roughness parameter	Hapke mean slope angle (°)
1	3	1	100	36.8 ± 0.4	0.56 ± 0.01	1.18 ± 0.01	0.82 ± 0.01	55.9 ± 1.0	0.331 ± 0.006	42.6 ± 0.8
↪	↪	↪	↪ 10% noise	36.6 ± 0.9	0.56 ± 0.03	1.18 ± 0.01	0.82 ± 0.01	56.5 ± 1.8	0.330 ± 0.006	42.4 ± 0.8
↪	↪	↪	↪ 50% noise	37.6 ± 0.4	0.59 ± 0.01	1.15 ± 0.01	0.85 ± 0.01	52.4 ± 1.3	0.330 ± 0.004	42.4 ± 0.5
1	3	1	50	36.3 ± 0.3	0.55 ± 0.01	1.16 ± 0.003	0.84 ± 0.003	53.6 ± 0.5	0.322 ± 0.004	41.6 ± 0.5
1	3	1	200	38.1 ± 0.3	0.60 ± 0.02	1.19 ± 0.01	0.81 ± 0.01	58.0 ± 1.2	0.333 ± 0.003	42.8 ± 0.4
1	3	1	300	38.9 ± 0.3	0.63 ± 0.01	1.18 ± 0.01	0.82 ± 0.01	56.4 ± 1.6	0.329 ± 0.008	42.3 ± 1.0
1.5	3	1	100	36.2 ± 0.2	0.54 ± 0.01	1.14 ± 0.02	0.86 ± 0.02	51.2 ± 2.6	0.314 ± 0.003	40.1 ± 0.4
2	3	1	100	36.0 ± 0.2	0.54 ± 0.01	1.14 ± 0.01	0.86 ± 0.01	50.5 ± 1.8	0.304 ± 0.003	39.5 ± 0.4
3	3	1	100	34.6 ± 0.6	0.50 ± 0.01	1.12 ± 0.02	0.88 ± 0.02	46.7 ± 3.2	0.287 ± 0.010	37.6 ± 1.3
1	1 (no erosion)	1	100	37.9 ± 0.1	0.60 ± 0.003	1.28 ± 0.04	0.72 ± 0.04	68.4 ± 4.2	0.343 ± 0.003	43.8 ± 0.4
1	5	1	100	36.8 ± 0.2	0.56 ± 0.01	1.14 ± 0.01	0.86 ± 0.01	51.0 ± 1.1	0.310 ± 0.005	40.2 ± 0.6
1	3	2	100/2 → 50	37.0 ± 0.8	0.57 ± 0.02	1.20 ± 0.02	0.80 ± 0.02	59.5 ± 2.0	0.333 ± 0.015	42.8 ± 1.9
1	3	2	100	37.3 ± 0.6	0.58 ± 0.02	1.21 ± 0.04	0.79 ± 0.04	59.6 ± 4.5	0.328 ± 0.011	42.2 ± 1.4
1	3	4	100/4 → 25	36.6 ± 0.7	0.56 ± 0.02	1.22 ± 0.01	0.78 ± 0.01	61.1 ± 1.2	0.328 ± 0.013	42.2 ± 1.7
1	3	4	100	37.4 ± 0.6	0.58 ± 0.02	1.29 ± 0.04	0.71 ± 0.04	69.0 ± 4.7	0.340 ± 0.008	43.6 ± 1.0
1	3	8	100/8 → 12.5	35.4 ± 1.7	0.52 ± 0.05	1.18 ± 0.06	0.82 ± 0.06	55.3 ± 8.7	0.292 ± 0.034	38.2 ± 4.4
1	3	16	100/16 → 6.25	32.0 ± 3.3	0.43 ± 0.09	1.12 ± 0.04	0.88 ± 0.04	46.8 ± 8.3	0.239 ± 0.025	32.4 ± 3.4

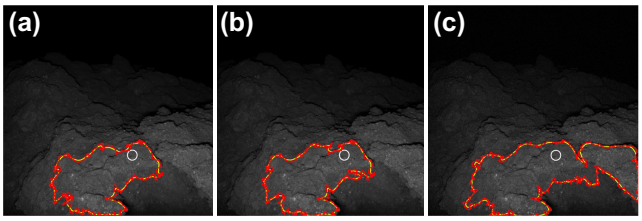

Figure 8. The effect of noise on growing a region in the middle of the image. The white, red, and yellow outlines represent the staring region from with the growing algorithm started (compare with Fig. 5a), rough contour and reference contour. (a) Original image, (b) additive noise of 10 per cent of the mean pixel value, (c) additive noise of 50 per cent of the mean pixel value. Note that the grown region approaches the image boundary on the right in (c) that causes a smaller fractal dimension.

The standard deviation multiplier is used to define the cut-off value for the growing region. All pixels with values lying within the mean plus/minus the standard deviation times its multiplier of the starting region are considered for growing the region. Changing the standard deviation multiplier results in different cut-off values with larger regions for larger multipliers. All roughness values show a decrease in roughness with increasing standard deviation multiplier. The larger the standard deviation multiplier, the larger are the grown regions and the distances to the camera they cover. Particularly at a large distance from the camera, the brightness gradient is smaller and borders of the grown region are smoother, which is represented in the lower roughness values. Also, boundaries that align with the image frame and that were not taken out of consideration, further smooth the roughness values. It is therefore advisable to use a small standard deviation multiplier and constrain the grown region to a small area.

Before determining the roughness of the grown region, a mathematical closing operation was applied to the boundary to remove any roughness introduced by inclusions, local surface tilts or image noise. The standard size of the structural element was 3 pixels. A smaller (1 pixel) and larger (5 pixels) structural element resulted in a higher and lower roughness, respectively, for all roughness values. This trend is expected because the size of the structural element removes any roughness on the scale of the structural element or smaller. Consequently, the larger the structural element, the smoother is the boundary and the lower the roughness. A structural element of 3 pixels, which is the approximate size of the inclusions and also removes blurriness and noise on the one pixel scale, is therefore the best choice for the size of the structural element.

Finally, we investigated the effect of the image scale by artificially decreasing the pixel resolution. For this, we reduced the image pixel resolution by averaging the pixel values within cells of 2 × 2, 4 × 4, 8 × 8, and 16 × 16 original pixels. We also explored the effect of decreasing the smoothing factor of the reference contour with the according image pixel resolution factor that maintains the spatial scale of the smoothing at about 2 cm. Dividing the smoothing factor by the image pixel resolution factor generally results in smaller roughness values because the smoothed reference contour approaches the shape of the rough boundary contour which naturally decreases the roughness relative to the reference contour. The only exception can be observed at a small-scale roughness parameter and deduced Hapke mean slope angle at an image pixel resolution factor of 2. Here, the roughness of the adjusted smoothing factor (divided by the image pixel resolution factor of 2) is larger. Nevertheless, since the values agree within their 1σ standard deviation, these values can be considered outliers.

For large image pixel resolution factors (8 and 16), all roughness values decrease with decreasing image resolution (e.g. increasing image resolution factors). At these low image resolutions, the grown regions only exist of a few pixels and the boundary contour is comparatively smooth accordingly. However, when considering the adjusted smoothing of the reference contour (e.g. maintaining the spatial scale of the smoothing for the reference contour by dividing the smoothing factor of the reference contour by the image pixel resolution factor), the roughness values do not peak at the highest pixel resolutions, but at an image pixel resolution factor of 2 for the RMS-slope, hemispherical crater density, small-scale roughness parameter, and Hapke mean slope angle and at an image pixel resolution of 4 for the fractal dimension, Hurst exponent, and JRC. This observation is probably caused by a few very bright boundary pixels (e.g. bright inclusions). Given the method of artificially reducing the image resolution by averaging the values in a given cell (e.g. 2 × 2 and 4 × 4), such pixels affect the boundary roughness on a larger scale when the image resolution is decreased. However, this roughness will not be removed by the subsequent erosion procedure as it is the case for the original image because its structural element is on the scale of or smaller than the image resolution. Thus, the effect of an increased roughness for a slightly reduced image resolution is probably an effect of the methods applied rather than a natural observation.

Following the analysis above, we conclude that the following parameters are most suitable for our subsequent analysis of Ryugu's (Section 5.2) and Churyumov–Gerasimenko's (Section 5.3) small-scale roughness derived from *in situ* images: smoothing factor of reference contour = 100, standard deviation multiplier = 1, size of structural element = 3, and image pixel resolution = 1.

5.2 Ryugu roughness

Fig. 5(a) shows the location of the five circular starting regions from which the growing algorithm was started in five different locations (structures) on Ryugu. According to their location, they are labelled back right, cave, front right, left-hand side, and middle. Table 2 lists the roughness parameters for the five regions in the MasCam image of Ryugu. For all structures, the approximate pixel resolution in horizontal and vertical direction is 0.2 mm, but depending on the local topography it varies slightly (Table 3).

In addition to the roughness values derived from the MasCam image using our new method, we also extracted the roughness values using shape models from MasCam and ONC. The region on Ryugu's rock which was observed by MARA was additionally evaluated for comparison with thermally derived roughness parameters (Table 2).

The values for the RMS-slope of the five regions imaged by MasCam on Ryugu determined with the above described method is larger than the RMS-slope of the global image derived with the same method. The values derived from the MasCam shape model is in between these two values. At the location of MARA's footprint on the Ryugu rock the RMS-slope is smallest, possibly caused by the comparatively flat local topography. The approximate roughness derived by fitting thermal measurements to the MARA night time data yields a similar value to the geometrically derived RMS-slope of this region. The shape model's RMS-slopes are generally smoother than the RMS-slope derived with our new method as they have a lower spatial resolutions compared to the image they are derived from and particularly steep slopes are averaged out. Consequently, the ONC shape model with a resolution of 20 cm has the lowest RMS-slope. The hemispherical crater density is proportional to the squared RMS-slope (equation 3) and thus shows the same trend.

Table 2. Parameters describing the roughness of Ryugu derived from different data sets.

Data set	Method	RMS slope (°)	Hemispherical crater density	Fractal dimension	Hurst exponent	JRC	Small scale roughness parameter	Hapke mean slope angle (°)
ONC shape model of 50 m × 50 m around MASCOT landing site, spatial resolution of ∼20 cm (124000 facets)	Spencer (1990), from profiles	26.7	0.3	1.008 ± 0.003	0.992 ± 0.003	14.1 ± 2.7	0.128	20.3
MasCam shape model, spatial resolution of ∼3 mm (14111 facets)	Spencer (1990), from profiles	34.9	0.51	1.011 ± 0.006	0.989 ± 0.006	16.4 ± 3.8	0.321	41.4
MasCam shape model of MARA's footprint with spatial resolution of ∼3 mm (4711 facets)	Spencer (1990)	26.2	0.28				0.141	21.7
MARA 8–12 μm filter daytime measurement	Thermal fitting	28.6	0.34					
MasCam image back right	This work[a]	35.4 ± 0.3	0.52 ± 0.01	1.11 ± 0.01	0.89 ± 0.01	46.3 ± 2.2	0.279 ± 0.003	36.8 ± 0.4
MasCam image cave	This work[a]	38.1 ± 0.9	0.60 ± 0.03	1.19 ± 0.02	0.81 ± 0.02	57.4 ± 2.7	0.342 ± 0.010	43.7 ± 1.3
MasCam image front right	This work[a]	34.9 ± 1.4	0.51 ± 0.04	1.11 ± 0.01	0.89 ± 0.01	45.6 ± 1.8	0.293 ± 0.015	38.3 ± 2.0
MasCam image front left	This work[a]	37.6 ± 0.3	0.59 ± 0.01	1.20 ± 0.04	0.80 ± 0.04	58.7 ± 4.4	0.330 ± 0.007	42.4 ± 0.9
MasCam image middle	This work[a]	36.8 ± 0.4	0.56 ± 0.01	1.18 ± 0.01	0.82 ± 0.01	55.9 ± 1.0	0.331 ± 0.006	42.6 ± 0.8
MasCam image mean	This work[a]	36.6 ± 1.4	0.56 ± 0.04	1.16 ± 0.04	0.84 ± 0.04	52.8 ± 6.3	0.315 ± 0.027	40.8 ± 3.5
ONC global image (red)	This work[a]	32.9 ± 2.2	0.45 ± 0.06	1.08 ± 0.02	0.92 ± 0.02	38.8 ± 4.0	0.263 ± 0.038	35.0 ± 5.1
ONC global image (blue)	This work[a]	32.0 ± 1.5	0.43 ± 0.04	1.08 ± 0.03	0.92 ± 0.03	39.4 ± 6.1	0.251 ± 0.022	33.7 ± 3.0

Notes. [a]The average contour was derived by smoothing with a running mean of 100, the standard deviation multiplier for the region growing method was set to 1 and all neighbours were considered. Outline indentations in the order of the bright inclusion size (3 pixels across) were removed from the high-resolution images. The errors are the 1σ standard deviation derived from five locally varying starting regions and, where deduced from other values, were derived via standard error propagation. The outlines of the global images were not smoothed.

Table 3. Approximate distance of the structures on Ryugu from the camera and the according approximate pixel resolutions in horizontal and vertical direction with reference to the image frame.

Region	Approximate distance from camera (cm)	Pixel resolution horizontal (mm)	Pixel resolution vertical (mm)
Back right	27.9	0.25	0.25
Cave	26.5	0.23	0.21
Front right	24.7	0.21	0.20
Front left	22.5	0.19	0.17
Middle	24.9	0.23	0.211

The fractal dimension, Hurst exponent, and JRC also show an increased roughness with decreasing spatial resolution of the data set. The only exception to this trend is found for the small-scale roughness parameter and the deduced Hapke mean slope angle. Here, the mean roughness of the five regions imaged by MasCam at a spatial resolution of 0.2 mm is slightly smaller than the roughness derived from the MasCam shape model at a spatial resolution of ∼3 mm. Nevertheless, the deviation is smaller than the error of the roughness values and is thus not significant.

With the exception of the location in the front right of the MasCam image, all roughness values derived with our method have a relatively small standard deviation (Table 2). The front right part of the image is close to the bottom right corner of the image that constrained the growing region. Because the image boundary is a straight line, the roughness of a grown region reaching the image boundary is underestimated and causes the comparatively small roughness values and large errors. The fractal dimension and deduced parameters are not affected as significantly by this because the straight image boundary introduces only a small number of smooth sections that have a negligible effect on the derivation of the fractal dimension (equation 9). Nevertheless, it should be avoided to extract roughness values too close to the image boundary.

5.3 67P/Churyumov–Gerasimenko roughness

We derived the roughness parameters from the ROLIS image of Churyumov–Gerasimenko in two locations, in the centre and at the left edge of the image (Fig. 5b, Table 4). As mentioned above, the image is slightly out of focus, which results in a systematic underestimation of the roughness as small-scale topography will not be resolved. Thus, the roughness reported on here is only a lower limit. In both locations, most roughness values are similar and agree within their errors. Only the small-scale roughness parameters and Hapke mean slope angles for both locations vary more significantly (Table 4). As seen by comparing the roughness parameters derived from the ONC and MasCam images, the roughness parameters derived from the global OSIRIS image of Churyumov–Gerasimenko are also generally smaller compared to the values derived from the high resolution images. It is also noticeable that due to the large image size (2048 × 2048 instead of 1024 × 1024 pixels) the errors of the roughness values derived from the OSIRIS image are comparatively small.

6 SMALL-SCALE SURFACE ROUGHNESS

6.1 Influence of spatial resolution, data sets, and method

Our method is sensitive to the decision made on the input parameters including the standard deviation multiplier of the circular region, the size of the structural element of the boundary contour, and the smoothing factor for the reference contour. Testing the influence of these input parameters, we conclude that the best set of parameters in order to achieve comparability between different images is a standard deviation multiplier of 1, a structural element size of 3, and a reference contour smoothing factor of 100. Using these values as a base, we can achieve comparability and reproducibility for this and future data sets. However, the parameters may have to be adjusted for possible future images depending on the data set and its quality. Varying point spread functions for different camera filters do not affect the results of the roughness values derived using our method. Image noise may influence the results on roughness with an increased noise level introducing larger roughness; however, the effect is not dramatic even for high noise levels, so that our method is capable of generating comparable results for a variety of images at similar spatial resolutions.

The roughness values of Ryugu derived from the MasCam and ONC shape models and images using the newly introduced method described in Section 4 shows that the roughness is dependent on the data set and its spatial resolution with higher spatial resolutions presenting lower roughness values. The same applies when comparing the roughness derived from the ROLIS and OSIRIS images at different spatial resolutions using our method. The spatially higher resolved images result in higher roughness. Because fractal surfaces have the characteristic that with decreased spatial resolution the total contour length decreases, it is expected that small-scale roughness remains unresolved at lower resolution.

When using the same data format and looking at the same planetary body, the roughness is spatially variable. For example, using the MasCam shape model, the roughness of the entire scene is much larger than the roughness of the MARA footprint area which is a subset of the entire scene (RMS-slope: 34.9° versus 26.2°, small-scale roughness parameter: 0.321 versus 0.141). The MasCam shape model shows that the MARA footprint is indeed on a relatively flat plateau surrounded by steeper slopes (Fig. 2a). Even though the five regions in the MasCam image have similar distances and orientations to the camera, our image-based method results in noticeably different roughness values in the five regions. The surface roughness has a significant influence on many remote sensing observations, but assuming a constant roughness value for an observation may not be advisable.

Nevertheless, considering the data sets from Ryugu and Churyumov–Gerasimenko used in this work, the roughness is higher for higher spatial resolution when considering the DTM-based and our image-based method separately. Generally, our image-based method derives higher roughness values compared to the DTM-based method that can be explained by the higher spatial resolution and the shape models' tendency to underestimate the roughness when meshing the topography. Extracting profiles from the DTMs to estimate the traditionally 2D roughness parameters, the fractal dimension, Hurst exponent, and JRC, results in even lower roughness values (Tatone & Grasselli 2010). Following this observation, it is not advisable to use 3D shape models for extracting these roughness parameters as they are significantly underestimated.

6.2 Roughness of Ryugu and 67P/Churyumov–Gerasimenko

Although the surface texture of undulating cauliflower-like features appears similar on asteroid Ryugu and comet Churyumov–Gerasimenko, the surface of Churyumov–Gerasimenko is slightly rougher compared to Ryugu on both the *in situ* sub-millimetre scale and the global scale. The fact that the spatial resolution of the Ryugu

Table 4. Parameters describing the roughness of comet 67P/Churyumov–Gerasimenko derived from a high-resolution ROLIS image and a global OSIRIS image. The reference contour was derived by smoothing with a running mean of 100, standard deviation multiplier for region growing method set to 1 and all neighbours considered. For comparability with the Ryugu analysis, outline indentations with a size of 3 pixels across where removed from the high resolution images. The outline of the global image was not smoothed.

Location	RMS slope (°)	Hemispherical crater density	Fractal dimension	Hurst exponent	JRC	Small scale roughness parameter	Hapke mean slope angle (°)
ROLIS image centre	38.3 ± 0.6	0.61 ± 0.02	1.18 ± 0.03	0.82 ± 0.03	56.4 ± 3.4	0.346 ± 0.015	44.2 ± 1.9
ROLIS image left edge	38.1 ± 0.7	0.60 ± 0.02	1.17 ± 0.02	0.83 ± 0.02	55.1 ± 2.2	0.323 ± 0.006	41.7 ± 0.3
OSIRIS global image	34.1 ± 0.2	0.48 ± 0.01	1.11 ± 0.003	0.89 ± 0.003	45.7 ± 0.5	0.277 ± 0.004	36.5 ± 0.5

MasCam image is higher (0.2 mm versus ∼0.8 mm) and that the Churyumov–Gerasimenko ROLIS image is slightly out of focus implies that comet Churyumov–Gerasimenko is indeed rougher than asteroid Ryugu because a higher spatial resolution and sharper image would result in higher resolved roughness. For example, the RMS-slope of Ryugu at a 0.8 mm spatial resolution (image pixel resolution factor of 4 in Table 1) is 36.6° ± 0.7°, 4.6 per cent less than the RMS-slope of 38.3° ± 0.6° for the same scale on Churyumov–Gerasimenko (in the image centre). The same observation can be made for the Hapke mean slope angle which is 4.7 per cent less.

The spatial resolution of the Ryugu and Churyumov–Gerasimenko global images is similar, but all roughness parameters at this scale also indicate that Churyumov–Gerasimenko is rougher than Ryugu. The RMS-slope and Hapke mean slope angle of Ryugu at the 2 m resolution global scale are 32.9° ± 2.2° and 35.0° ± 5.1°, respectively, 3.6 per cent and 4.3 per cent less than that of Churyumov–Gerasimenko (RMS-slope: 34.1° ± 0.2°, Hapke mean slope angle: 36.5° ± 0.5°). With the exception of the fractal dimension at the *in situ* scale, which is probably slightly distorted by the applied method as argued in Section 5.1, all roughness parameters show the same trend with Churyumov–Gerasimenko being between 2.8 per cent and 5.5 per cent rougher compared to Ryugu. However, given the comparatively large errors at this scale for Ryugu, the conclusion is less reliable than at smaller scales.

6.3 Roughness caused by sublimation of volatiles

Given that Ryugu is a rubble pile Cb-type asteroid (Sugita et al. 2019; Kitazato et al. 2019) and Churyumov–Gerasimenko is an active comet, differences in roughness can be expected. Laboratory experiments have shown that volatile outgassing under cometary conditions increases the near surface porosity and generates fluffy particles or aggregates from the sublimation residues that are ejected from the surface (Grün et al. 1993; Kossacki et al. 1997). The Rosetta mission at Churyumov–Gerasimenko confirmed the existence of fluffy aggregates in the size range of a 10–500 μm (Langevin et al. 2016) and 0.2–2.5 mm (Fulle et al. 2015), a scale comparable to the image resolution used in this work. It is probable that their fluffy nature is also preserved in Churyumov–Gerasimenko's near surface (Poch et al. 2016) and contribute to the observed rough texture of the comet. On the other hand, Ryugu has been reported to be neither pristine nor active and its surface materials, which were potentially compressed within the parent body and subsequently during a catastrophic impact event (Okada et al. 2020; Sugita et al. 2019), are likely more compacted and thus may show a lower roughness compared to Churyumov–Gerasimenko.

6.4 Roughness caused by micrometeoroid impacts

Surface roughness on the centimetre and millimetre scale may also be caused by micrometeoroid impacts, as was argued for the Moon (Bastin 1966) and observed on near-Earth asteroids Itokawa and Bennu (Miyamoto et al. 2007; Ballouz et al. 2020). As described in Section 2.1, the surface of Ryugu is characterized by cauliflower-like undulations of ∼1 cm that are covered with smaller undulations of approximately 2–3 mm. The smaller undulation size is also confirmed by our measurements of the fractal dimension, in which the contour is divided into sections by the intersection of the rough and reference contour. These intersections are approximately 2.5 mm long. Furthermore, impact experiments on to carbonaceous chondrite analogue materials simulating micrometeoroid bombardment show resemblance to the observed surface morphology of Ryugu and result in a mean surface slope (32°) similar to the one derived for Ryugu (Avdellidou et al. 2020).

To test if the cauliflower-like structures may be a result of spallation and compaction of micrometeoroid bombardment into a highly porous and low strength rock, we assume that a hypervelocity impact into a highly porous material can be assumed to be 10 times larger than the impactor (Tedeschi et al. 1995), thus a 250 μm particle would cause a 2.5 mm impact feature. Based on the Interplanetary Meteoroid Environment Model 2 by Soja et al. (2019), the mean impact speed of a 250 μm dust particle in a near Earth orbit is approximately 16 km s^{-1} and has an flux of ∼8 × 10^{-9} $m^{-2}s^{-1}$. Assuming that the rock imaged by MasCam has been exposed at the surface since Ryugu's formation [approximately 10^7 yr ago (Arakawa et al. 2020)], this flux results in about 1.6 × 10^5 accumulated impacts in the imaged 25 cm × 25 cm scene or 250 impacts per cm^2. This implies that the total area affected by an impact of this size is approximately 10 times larger than the area of the scene meaning that the surface should show traces of such impact cater features and that micrometeoroid bombardment plays a role in the formation of Ryugu's surface roughness. However, impactors of various sizes hit the surface and specifically smaller particle impacts occur much more frequently (e.g. ∼5 × 10^{-7} m^{-2} $s^{-1}$for 50 μm particles). They should erode larger crater features with time. For example, in the considered timeframe the total crater feature area of 50 μm impactors is about 30 times larger than the target area.

Further processes eroding the surface of airless bodies include solar weathering and thermal fatigue. It is possible that Ryugu's cauliflower-like texture represents an intrinsic property of the rock when exposed to multiple surface processes, including solar space weathering and thermal fatigue in addition to micrometeoroid bombardment. Given the different strength of regolith on differently classified objects and the expectation that thermal erosion of carbonaceous chondritic material is more efficient than thermal erosion of ordinary chondritic material (Delbo et al. 2014), the small-

scale surface morphology and roughness may vary between different bodies. These processes are most effective on asperities and round rock surfaces (Delbo et al. 2014; Gault, H"orz & Hartung 1972). Given that Ryugu is a product of a catastrophic impact and has been bombarded by meteoroids since its rocks should exhibit impact-induced intrinsic fracture patterns on various scales (Tomeoka, Yamahana & Sekine 1999) encouraging thermally induced foliation along them and possibly supporting the cauliflower-like texture. In contrast, the surface of Churyumov–Gerasimenko is renewed approximately every 6.5 yr when the comet passes its perihelion and ejects large amounts of its surface material. Micrometeoroid bombardment should therefore not play a significant role in the formation of surface roughness on Churyumov–Gerasimenko.

A combination of the above-mentioned processes and the differences in bulk material composition and texture is likely the cause for the observation that Churyumov–Gerasimenko is rougher than Ryugu.

7 DISCUSSION

It is challenging to relate the roughness of Ryugu and Churyumov–Gerasimenko to previously derived values on other planetary bodies and materials on the Earth because of the variations in applied methods, scales, and data sets. Nevertheless, to achieve a sense for their roughness, we will discuss a few values of other materials and planetary bodies.

The fractal dimension and derived JRC are acknowledged parameters used in geological sciences for the estimation of the peak shear strength of a material. Common values for the fractal dimension for typical rocks (quartz, granite, sandstone, limestone, shale) range between 1.05 and 1.19 (Pal et al. 2017). The best match for Ryugu ($D = 1.16 \pm 0.04$) as well as Churyumov–Gerasimenko ($D = 1.18 \pm 0.03$) appears to be the comparatively rough limestone investigated in their survey. On larger scales, the fractal dimension has been investigated for geologic features such as lava flows on the Earth ($D = 1.06-1.19$) as well as the Moon ($D = 1.20$; Bruno et al. 1992). Note that all comparative values have been derived with the box counting method. The application of different methods may have an influence on the derived values (Klinkenberg 1994), but the method used in this work yields the most reliable correlation with the JRC (Li & Huang 2015).

The JRC relates the shear peak strength and normal stress following equation (11). Although the assumption that Ryugu's rock is jointed due to its impact history seems reasonable, the JRC may not be an adequate parameter on Ryugu and Churyumov–Gerasimenko given the small gravitational field in which the rocks exist. The values presented in this work are guidance but do not claim that they represent the actual behaviour of rock on the small bodies.

The Hurst exponent has been derived for Eros and Itokawa, two small S-type asteroids previously visited by spacecraft, from laser ranging data. Over a range of 3 m–1 km the global Hurst exponent of Eros was found to range between 0.81 and 0.97 (Cheng et al. 2002; Susorney & Barnouin 2018) and from scales between 8 and 32 m the global Hurst exponent of Itokawa is 0.51 ± 0.07 (Susorney et al. 2019). The differences in roughness have been attributed to different geologic processes and internal structures of the two bodies, with Eros possessing a stronger intact interior with surface impact craters and Itokawa being a rubble pile asteroid with large variations in the geopotential and induced regolith migration as main surface process (Susorney et al. 2019). At a scale of 2 m, we derived a similar global Hurst exponent of Ryugu of 0.92 ± 0.02 [and Churyumov–Gerasimenko (0.89 ± 0.003)] to the one derived for Eros. Although Ryugu as a rubble pile asteroid should geologically resemble Itokawa more than Eros, it is possible that the discrepancy is caused by Ryugu's comparatively symmetric shape and the different boulder size distributions at this scale. Smaller boulders seem to be buried in the regolith on Ryugu and the different composition of Ryugu and Itokawa probably results in different sized impact fragments because S-type asteroid materials (ordinary chondrites) are stronger than C-type asteroid materials (carbonaceous chondrites; Popova et al. 2011; Michikami et al. 2019).

The RMS-slope has been retrieved from many data sets of planetary missions applying different methods and scales. Generally, the values range between 20° and 40° for airless bodies, but variations are common with scale and location. Thermal modelling is able to retrieve roughness estimates on the scale of the thermal skin depth (centimetre scale). The best-fitting RMS-slope of Ryugu at the Mascot landing deduced by a thermal model site is 28.6°. Similar investigations of Ceres and the Moon result in higher RMS-slopes of 40° (Davidsson et al. 2015; Müller et al. 1999; Spencer 1990) and 30°−39° (Rozitis & Green 2011; Shkuratov et al. 2000; Spencer 1990), respectively. Radar observations of slightly higher wavelength (decimetre scale) confirm these values (Mitchell et al. 1996). The comparatively high roughness has been attributed to a fine-grained regolith covered surface that, in contrast to Ryugu (Jaumann et al. 2019), is able to form on these objects with larger gravitational pull. The roughness from thermal measurements on Churyumov–Gerasimenko has been shown to be locally highly variable and covers the range from 16° to 44° (Marshall et al. 2018). Given the high variation in published values, our estimates of the RMS-slope of Ryugu ($36.6° \pm 1.4°$) and Churyumov–Gerasimenko ($38.3° \pm 0.6°$) agrees with these estimates.

The RMS deviation (difference in height between points separated by a constant distance/measuring length) of planetary bodies has also been derived from shape models and laser altimeters at different resolutions (Barnouin-Jha et al. 2008; Ermakov et al. 2019). The RMS deviation directly relates to the Hurst exponent and the RMS slope can be deduced from the RMS deviation at a given measuring length (Shepard et al. 2001). Unfortunately, on the spatial scales of the data sets investigated in this work (0.2 mm –2 m), there are no comparable data sets from any other planetary bodies to date.

Based on the stereophotogrammetric analysis of Apollo Lunar Surface Closeup Camera images, Helfenstein & Shepard (1999) were able to derive the RMS slope and Hapke roughness parameter for lunar soil on sub-millimetre scales. They found values of 16°−25° for the RMS-slope and 24°−27° for Hapke's mean slope angle of different regolith types (lunar mare, Fra Mauro regolith). Comparing these values with the stereophotogrammetrically derived shape model of Ryugu at slightly larger scales (3 mm), we find larger values of 34.9° and 26.2° (RMS-slope) for the entire rock and MARA footprint area, respectively. The Hapke mean slope angle of Ryugu for these two areas is 21.7° and 41.4°, slightly smaller and larger compared to the values derived from the Moon. Because the Moon's surface regolith is a fine-grained soil covering bare rock surfaces, which is not present on Ryugu, differences in roughness values are expected. This example illustrated how significantly these values can vary locally when using 3D shape models at small scales.

The Hapke mean slope angle is generally derived from photometric models and gives the roughness on a microscopic scale at which shadows influence photometric observations (Hapke 1984). In our work, the Hapke mean slope angle was derived from the small-scale roughness parameter (equation 6). Our values for the Hapke mean slope angle are generally high (Ryugu: $40.8° \pm 3.5°$, Churyumov–Gerasimenko: $44.2° \pm 1.9°$) compared with values derived from pho-

tometric analyses of Churyumov–Gerasimenko (19° ± 9°, Ciarniello et al. 2015) and comet Tempel 1 (16°−32°, Li et al. 2007). The same trend is observed for values from asteroids Eros (24°−28°, Clark et al. 2002; Li, A'Hearn & McFadden 2004), Itokawa (26°−38°, Kitazato et al. 2008; Tatsumi et al. 2018) and Ceres (18°−29°, Ciarniello et al. 2017; Li et al. 2019; Schröder et al. 2017b). The Hapke mean slope angle of Ryugu derived from photometric fitting was found to be 28° ± 6° (Tatsumi et al. 2020). The discrepancy between geometrically and photometrically derived mean slope angles has previously been explained for the Moon by Helfenstein & Shepard (1999). They suggest that below spatial resolutions of approximately 0.1 mm roughness may not be photometrically detectable. As we approach such scales in our investigation, this limitation may be applicable. Furthermore, by comparing geometrically and photometrically derived roughness values from an artificially generated terrain, Labarre, Ferrari & Jacquemoud (2017) showed that the Hapke mean slope angle systematically underestimates the surface roughness. They attribute this behaviour to the often unsuitable assumption of a Gaussian distribution of not too large slope angles and a moderately bright material. All the latter two assumptions are not valid for the scene observed on Ryugu and Churyumov–Gerasimenko and may thus explain the significantly higher value for the Hapke mean slope angle that we derive geometrically in this work.

8 CONCLUSIONS

Based on a newly developed image analysis technique suitable to extract surface roughness, we derived a set of roughness descriptors for asteroid Ryugu and comet Churyumov–Gerasimenko based on high-resolution images with 0.2 mm pixel^{-1} and ∼0.8 mm pixel^{-1} covering a scene of approximately 25 and 80 cm horizontal extent, respectively and two global images with 2 m spatial resolution. We complemented our survey with two local shape models of Ryugu at 3 mm and 20 cm spatial resolution. The roughness descriptors include the fractal dimension and the deduced Hurst exponent and JRC, the RMS-slope and derived hemispherical crater density, and the small-scale self-heating parameter and deduced Hapke mean slope angle. As a Cb-type asteroid and an active comet, Ryugu's and Churyumov–Gerasimenko's composition is expected to be different. However, the general cauliflower-like texture of both bodies visible in the high resolution *in situ* images appears similar. The structure on Ryugu is most likely linked to erosion via micrometeoroid bombardment, solar weathering, and thermal fatigue of a compacted impact rock fragment, whereas on Churyumov–Gerasimenko sublimation-driven erosion of a volatile-rich regolith is potentially the most dominant process for forming surface roughness. We suggest that these different processes and compositions combined are represented by the slightly rougher descriptors (2.8–5.5 per cent) for Churyumov–Gerasimenko than for Ryugu on the investigated scales.

ACKNOWLEDGEMENTS

We thank the Hayabusa2 and MASCOT as well as the Rosetta and Philae teams for making this work possible. KO and RP gratefully acknowledge the financial support and endorsement from the German Aerospace Center (DLR) Management Board Young Research Group Leader Program and the Executive Board Member for Space Research and Technology. This study was supported by Japanese Society for the Promotion of Science (JSPS) International Planetary Network. We thank an anonymous reviewer for the helpful and productive comments.

DATA AVAILABILITY

All data derived in this work are incorporated in the article. Images from the Hayabusa2 mission will be published in the Data Archives and Transmission System at https://www.darts.isas.jaxa.jp/pub/hayabusa2/onc_bundle/. The image from the Rosetta mission is available at ESA's Planetary Science Archive at https://archives.esac.esa.int/psa/ and can be accessed by searching for 'OSIRIS [instrument]" (Product identifier: N20140806T012001282ID30F28). The original ROLIS image is available at ftp://psa.esac.esa.int/pub/mirror/INTERNATIONAL-ROSETTA-MISSION/ROLIS/RL-C-ROLIS-2-FSS-V1.0/DATA/ (Product identifier: ROL_FS2_141113001408_336_04) and was processed using the method described in Schröder et al. (2017a) and the polynomial coefficients provided as supplementary material to this publication. The MasCam image is available at http://europlanet.dlr.de/Hayabusa2/MASCAM/index.html (Product identifier: F1087378791_701_29464_r1). The digital terrain models shown in Fig. 2 are available at http://europlanet.dlr.de/Hayabusa2/MASCOT/index.html under the according publication.

REFERENCES

Arakawa M. et al., 2020, Science, 368, 67
Avdellidou C. et al., 2020, Icarus, 341, 113648
Ballouz R.-L. et al., 2019, in Asteroid Science 2019. Lunar and Planetary Institute, p. 2123
Barnouin-Jha O. S. et al., 2008, Icarus, 198, 108
Barton N., 1976, Int. J. Rock Mech. Mining Sci. Geomech. Abstr., 13, 255
Barton N., Choubey V., 1977, Rock Mech. Felsmechanik Méc. Roches, 10, 1
Bastin J. A., 1966, Nature, 212, 171
Bibring J.-P. et al., 2015, Science, 349, aab0671
Bruno B. C., Taylor G. J., Rowland S. K., Lucey P. G., Self S., 1992, Geophys. Res. Lett., 19, 305
Buhl D., Welch W. J., Rea D. G., 1968, J. Geophys. Res., 73, 5281
Cai Y., Tang H.-m., Wang D.-j., Wen T., 2018, Math. Probl. Eng., 2018, 1
Cheng A. F. et al., 2002, Icarus, 155, 51
Ciarniello M. et al., 2015, A&A, 583, 1
Ciarniello M. et al., 2016, MNRAS, 462, S443–S458
Ciarniello M. et al., 2017, A&A, 598, 1
Clark B. E. et al., 2002, Icarus, 155, 189
Davidsson B. J. R., Rickman H., 2014, Icarus, 243, 58
Davidsson B. J. R., Gutiérrez P. J., Rickman H., 2009, Icarus, 201, 335
Davidsson B. J. R. et al., 2015, Icarus, 252, 1
Davidsson B. J. R. et al., 2016, A&A, 592, 1
Delbo M. et al., 2014, Nature, 508, 233
Ermakov A. I., Kreslavsky M. A., Scully J. E. C., Hughson K. H. G., Park R. S., 2019, J. Geophys. Res., 124, 14
Fuchs L. H., Olsen E., Jensen K. J., 1973, Smithsonian Contrib. Earth Sci., 10, 1
Fulle M. et al., 2015, ApJ, 802, L12
Gault D. E., H"orz F., Hartung J. B., 1972, in Proceedings of the 3rd Lunar and Planetary Science Conference. The MIT Press, p. 2713
Gonzalez R. C., Woods R. E., 2018, Morphological Image Processing, 4th edn. Pearson, p. 694
Gounelle M., Zolensky M. E., 2014, Meteorit. Planet. Sci., 49, 1769
Grott M. et al., 2019, Nat. Astron., 3, 971
Grün E. et al., 1993, J. Geophys. Res. , 98, 15091
Hamm M., 2019, PhD thesis, Freie Univ. Berlin
Hapke B., 1981, J. Geophys. Res., 86, 3039
Hapke B., 1984, Icarus, 59, 41
Helfenstein P., 1988, Icarus, 73, 462
Helfenstein P., Shepard M. K., 1999, Icarus, 141, 107
Hiroi T., Peters C. M., 1991, in Proceedings of Lunar and Planetary Science. Lunar and Planetary Institute, p. 313

Ho T.-M. et al., 2017, Space Sci. Rev., 208, 339
Huang S. L., Oelfke S. M., Speck R. C., 1992, Int. J. Rock Mech. Min. Sci. Geomech. Abstr., 29, 89
Jaumann R. et al., 2017, Space Sci. Rev., 208, 375
Jaumann R. et al., 2019, Science, 365, 817
Jiang Y., Li B., Tanabashi Y., 2006, Int. J. Rock Mech. Min. Sci., 43, 837
Jorda L. et al., 2016, Icarus, 277, 257
Kameda S. et al., 2017, Space Sci. Rev., 208, 17
Keller H. U. et al., 2007, Space Sci. Rev., 128, 433
Keller H. U. et al., 2015, A&A, 583, 1
Kitazato K. et al., 2008, Icarus, 194, 137
Kitazato K. et al., 2019, Science, 364, 272
Klinkenberg B., 1994, Math. Geol., 26, 23
Knapmeyer M., Fischer H.-H., Knollenberg J., Seidensticker K. J., Thiel K., Arnold W., Faber C., M"ohlmann D., 2018, Icarus, 310, 165
Kossacki K. J., K"omle N. I., Leliwa-Kopystynski J., Kargl G., 1997, Icarus, 128, 127
Labarre S., Ferrari C., Jacquemoud S., 2017, Icarus, 290, 63
Lagerros J. S. V., 1996, A&A, 310, 1011
Lagerros J. S. V., 1997, A&A, 325, 1226
Lagerros J. S. V., 1998, A&A, 332, 1123
Langevin Y. et al., 2016, Icarus, 271, 76
Lee S. D., Lee C. I., Park Y., 1997, Int. J. Rock Mech. Min. Sci., 34, 174
Li Y., Huang R., 2015, Int. J. Rock Mech. Min. Sci., 75, 15
Li J., A'Hearn M. F., McFadden L. A., 2004, Icarus, 172, 415
Li J.-Y. et al., 2007, Icarus, 187, 41
Li J.-Y. et al., 2019, Icarus, 322, 144
Mandelbrot B., 1967, Science, 156, 636
Marshall D. et al., 2018, A&A, 616, 1
Michikami T. et al., 2019, Icarus, 331, 179
Mitchell D. L. et al., 1996, Icarus, 124, 113
Miyamoto H. et al., 2007, Science, 316, 1011
Morota T. et al., 2020, Science, 368, 654
Mottola S., Arnold G., Grothues H.-G., Jaumann R., Michaelis H., Neukum G., Bibring J.-P., 2007, Space Sci. Rev., 128, 241
Mottola S. et al., 2015, Science, 349, aab0232.1–4
Müller T. G., Lagerros J. S. V., Burgdorf M., Lim T., Morris P. W., Salama A., Schulz B., Vandenbussche B., 1999, in Cox P., Kessler M., Danesy D., eds, ESA Special Publication, Vol. 427, The Universe as Seen by ISO. ESA Special Publication, p. 141
Odling N. E., 1994, Rock Mech. Rock Eng., 27, 135
Okada T. et al., 2020, Nature, 579, 518
Pal S. K., Rao K. U. M., Kumar P. S., Rajasekar R., 2017, Arch. Metall. Mater., 62, 1787
Poch O., Pommerol A., Jost B., Carrasco N., Szopa C., Thomas N., 2016, Icarus, 267, 154
Popova O., Borovicka J., Hartmann W. K., Spurný P., Gnos E., Nemtchinov I., Trigo-Rodríguez J. M., 2011, Meteorit. Planet. Sci., 46, 1525
Poulet F. et al., 2016, MNRAS, 462, S23
Preusker F. et al., 2015, A&A, 583, A33
Preusker F. et al., 2019, A&A, 632, 1
Reeves M. J., 1985, Int. J. Rock Mech. Min. Sci. Geomech. Abstr., 22, 429
Rost E., Hecker C., Schodlok M. C., Van der Meer F. D., 2018, Minerals, 8, 1
Rozitis B., Green S. F., 2011, MNRAS, 415, 2042
Rozitis B., Green S. F., 2012, MNRAS, 423, 367
Rozitis B., Green S. F., 2013, MNRAS, 433, 603
Scholten F. et al., 2019, A&A, 632, 1
Schr"oder S. E. et al., 2017a, Icarus, 285, 263
Schr"oder S. E. et al., 2017b, Icarus, 288, 201
Schr"oder S. E. et al., 2020, Planet. Sci. J., Submitted
Shepard M. K., Campbell B. A., 1998, Icarus, 134, 279
Shepard M. K., Campbell B. A., Bulmer M. H., Farr T. G., Gaddis L. R., Plaut J. J., 2001, J. Geophys. Res., 106, 32777
Shkuratov Y., Stankevich D., Sitko M. L., Sprague L. A., 2000, in Sitko M. L., Sprague A. L., Lynch D. K., eds, ASP Conf. Ser., Vol. 196, Thermal Emission Spectroscopy and Analysis of Dust, Disks, and Regoliths. Astron. Soc. Pac., San Fransisco, p. 211
Soja R. H. et al., 2019, A&A, 628, 1
Spencer J. R., 1990, Icarus, 83, 27
Spohn T. et al., 2015, Science, 349, aab0464.1–4
Steinbrügge G., Stark A., Hussmann H., Wickhusen K., Oberst J., 2018, Planet. Space Sci., 159, 84
Steinbrügge G. et al., 2020, Icarus, 343, 113669
Sugita S. et al., 2019, Science, 364, 1
Susorney H. C. M., Barnouin O. S., 2018, Icarus, 314, 299
Susorney H. C. M., Johnson C. L., Barnouin O. S., Daly M. G., Seabrook J. A., Bierhaus E. B., Lauretta D. S., 2019, Icarus, 325, 141
Tatone B. S. A., Grasselli G., 2009, Rev. Sci. Instrum., 80, 125110.1–10
Tatone B. S. A., Grasselli G., 2010, Int. J. Rock Mech. Min. Sci., 47, 1391
Tatsumi E. et al., 2018, Icarus, 311, 175
Tatsumi E. et al., 2020, A&A, 639, 1
Tedeschi W. J., Remo J. L., Schulze J. F., Young R. P., 1995, Int. J. Impact Eng., 17, 837
Tomeoka K., Yamahana Y., Sekine T., 1999, Geochim. Cosmochim. Acta, 63, 3683
Tse R., Cruden D. M., 1979, Int. J. Rock Mech. Min. Sci. Geomech. Abstr., 16, 303
Ulamec S. et al., 2016, Acta Astron., 125, 80
Watanabe S. et al., 2019, Science, 364, 268
Watanabe S.-i., Tsuda Y., Yoshikawa M., Tanaka S., Saiki T., Nakazawa S., 2017, Space Sci. Rev., 208, 3
Xie H.-P., Pariseau W. G., 1994, Sci. China B, 37, 1516
Xu Y. F., Sun D. A., 2005, Géotechnique, 55, 691
Yano H. et al., 2006, Science, 312, 1350
Zahouani H., Vargiolu R., Loubet J. L., 1998, Math. Comput. Modelling, 28, 517

This paper has been typeset from a TEX/LATEX file prepared by the author.